ELSEVIER

Volume 184, Issue 12, December 2011

JOURNAL OF SOLID STATE CHEMISTRY

www.elsevier.com/locate/jssc

CONTENTS

Abstracted/indexed in BioEngineering Abstracts, Chemical Abstracts, Coal Abstracts, Current Contents/Physics, Chemical, & Earth Sciences, Engineering Index, Research Alert, SCISEARCH, Science Abstracts, and Science Citation Index. Also covered in the abstract and citation database SciVerse SCOPUS®. Full text available on SciVerse ScienceDirect®.

Regular Articles

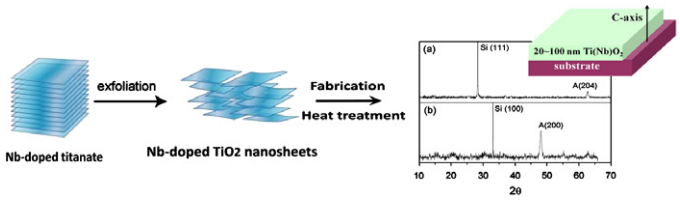

Layered Nb-titanates are appropriate precursors for formation of highly oriented Nb-substituted anatase thin films via delamination, reconstruction and subsequent heat treatment.

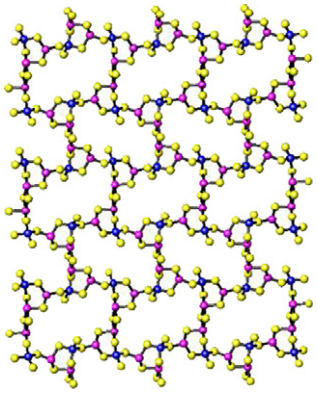

$[Ge(C_2N_2H_8)_3][GeSb_2S_6]$ is a mixed valent germanium compound that contains $[GeSb_2S_8]^{6-}$ units cross linked through Sb_2S_2 units to generate layers.

Regular Articles—Continued

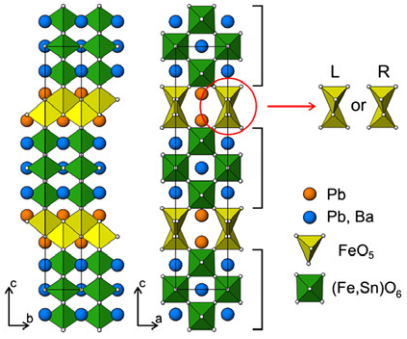

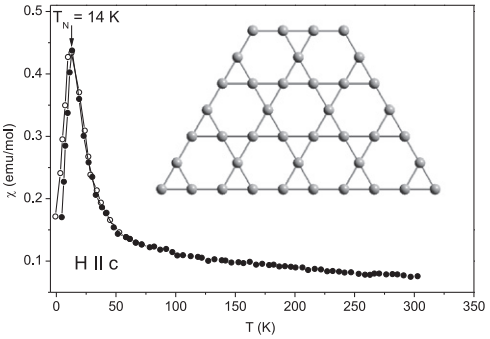

Single crystals of novel magnetoplumbite $BaSn_6Co_6O_{19}$ have been characterized.

Continued

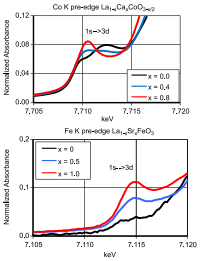

Co K and Fe K pre-edge of $La_{1-x}Ca_xCoO_{3-\delta}$ and $La_{1-x}Sr_xFeO_{3-\delta}$ perovskites one of the evidences in favor of $\delta = x/2$ for the Co-perovskites and $\delta = 0$ for the Fe-perovskites.

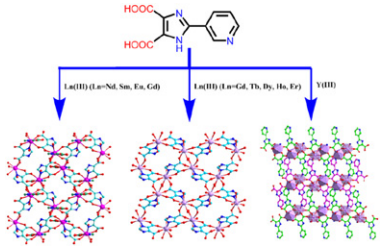

Structure variation of ten *Ln*(III) complexes is attributed to the lanthanide contraction effect and various coordination modes of H_3PyIDC ligands. Moreover, photoluminescent properties and thermal behaviors of selected complexes were investigated.

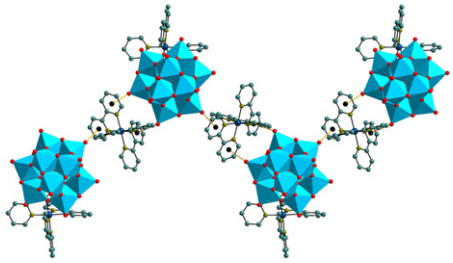

Two three-dimensional framework solids are constructed from polyoxoanions and ruthenium-organic complexes through non-covalent interactions.

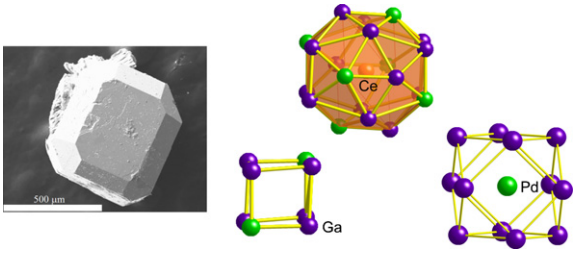

Single crystals of $CePd_3Ga_8$ have been synthesized from Ga flux. This new compound is the first rhombohedral variant of the cubic $BaHg_{11}$ structure type.

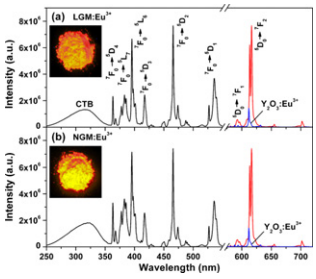

The intensity of the red emission of $M_2(Gd_{1-x}Eu_x)_4(MoO_4)_7$ (M = Li, Na) phosphors with the optimal compositions is about five times higher than that of Y_2O_3:Eu^{3+}.

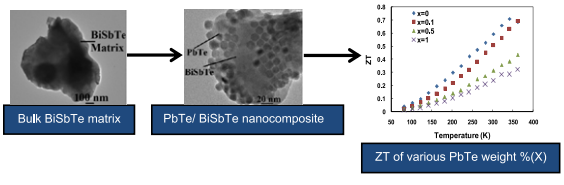

PbTe nanoparticles introduced into p-type Bi_2Te_3 by incipient wetness results in decreased lattice thermal conductivity, but also acts as an electronic dopant, resulting in an overall decrease in thermoelectric performance.

Photoelectrochemical water splitting and simultaneous photoelectrocatalytic degradation of organic pollutant on highly smooth and ordered TiO_2 nanotube arrays
Hongjun Wu and Zhonghai Zhang
page 3202

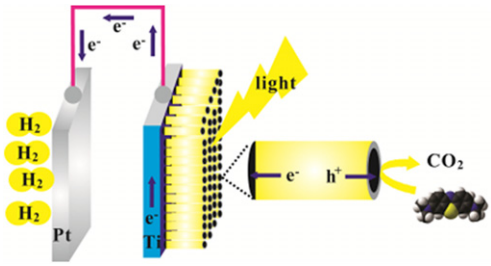

The photoelectrochemical water splitting for hydrogen generation and simultaneous photoelectrocatalytic degradation of organic pollutant (methylene blue) were achieved on TiO_2 nanotube electrodes with double purposes of environmental protection and renewable energy production under illumination of simulated solar light.

Evidence for transition from polaron to bipolaron conduction in electroactive $Li_xCr_{0.11}V_2O_{5.16}$ powders: A dynamic study from 10 to 10^{10} Hz
J.C. Badot and O. Dubrunfaut
page 3208

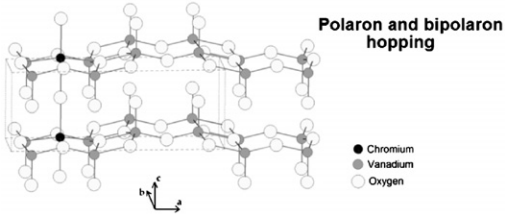

Schematic structure of $Cr_{0.11}V_2O_{5.16}$.

Magnetic and electronic properties of nanocrystalline $Gd_3Fe_5O_{12}$ garnet
H. Lassri, E.K. Hlil, S. Prasad and R. Krishnan
page 3216

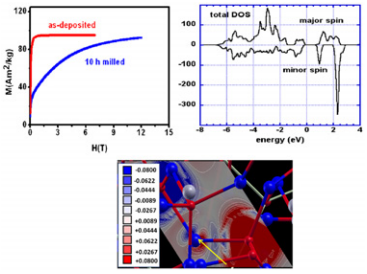

Random anisotropy fields, random anisotropy constant, substantial interstitial magnetism as well as magnetic quadrupolar feature on oxygen are determined from magnetization, theoretical random magnetic anisotropy model and FLAPW calculations in nanocrystalline Gadolinium Iron Garnet (GdIG).

Seeking the optimal $LaTaO_4$:Eu phosphor
Grant C. Bleier, May Nyman, Lauren E.S. Rohwer and Mark A. Rodriguez
page 3221

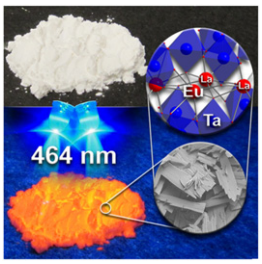

Eu-substituted lanthanum orthotantalates, $LaTaO_4$:Eu, are excellent red phosphors. They exhibit up to 83% quantum-yield emission under blue light excitation, optimized through both 'soft chemical processing' and polymorph purity.

Unusual oxidation states give reversible room temperature magnetocaloric effect on perovskite-related oxides $SrFe_{0.5}Co_{0.5}O_3$
C. Yin, Q. Liu, R. Decourt, M. Pollet, E. Gaudin and O. Toulemonde
page 3228

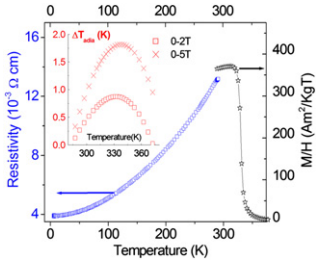

Moderate but reversible magnetocaloric properties are associated with the 2nd order paramagnetic to ferromagnetic phase transition exhibited at 330 K. A metal-like behavior is seen for the first time on the ferromagnetic regime.

Cu–Ce–O mixed oxides from Ce-containing layered double hydroxide precursors: Controllable preparation and catalytic performance
Zheng Chang, Na Zhao, Junfeng Liu, Feng Li, David G. Evans, Xue Duan, Claude Forano and Marie de Roy
page 3232

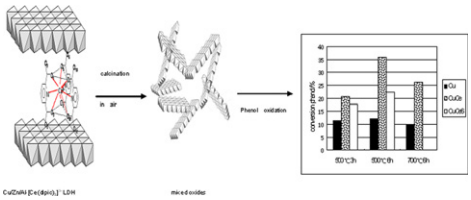

Cu–Ce–O mixed oxides calcined from $[Ce(dipic)_3]^{3-}$- intercalated Cu/Zn/Al layered double hydroxides were synthesized and displayed good catalytic performances in phenol oxidation due to the Cu–Ce interactions.

Continued

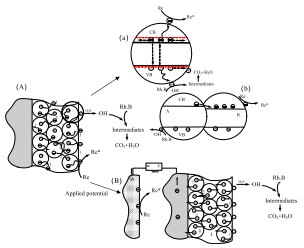

Photophysical chemistry processes in as-prepared TiO_2 photoelectrodes. Overall scheme of TiO_2 photoelectrodes: (A) movement of photoelectrons and holes without bias potentials; (B) movement of photoelectrons and holes at applied bias potentials; (a) and (b) were the transmission of photogenerated electrons and holes of local enlargement of (A) (black open circle): (a) photoelectrons movement in P-TiO_2 photoelectrodes and La-TiO_2 photoelectrodes, the red dot line denotes the top of valence band (VB) and the bottom of conduction band (CB) of pure photoelectrodes; (b) photoelectrons movement in P-160 and La-160 TiO_2 photoelectrodes (mixed crystal phase). The number refers to as follows: (1) transmission process of photoelectrons and holes; (2) recombination process of photoelectrons and holes. Arrows represent the moving direction of photoelectrons.

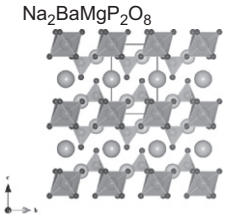

Emission properties of $Na_2MMgP_2O_8$ (M: Ba, Sr, Ca) are discussed from the viewpoint of the crystal structure solved by X-ray powder diffraction technique.

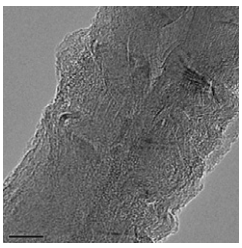

Functionalized CNTs were enwrapped by polymer chains with thickness of several nanometers, forming core–shell structures with CNTs at the center.

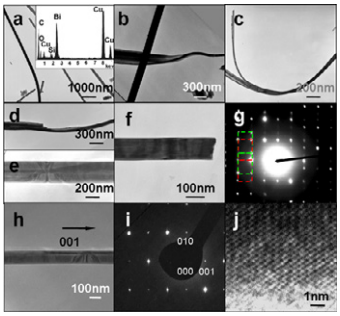

TEM images, EDS, and electron diffraction pattern of bismuth nanobelts.

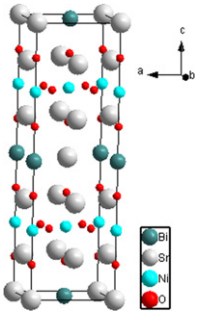

View of the structure of new $Sr_5BiNi_2O_{9.6}$ oxide.

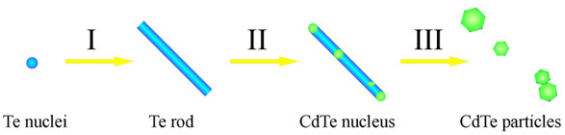

Firstly, Te nucleated and grew into nanorods in the presence of $EDTA^{2-}$. Then CdTe nucleus began to emerge on Te nanorods and finally monodispersed CdTe nanoparticles were obtained.

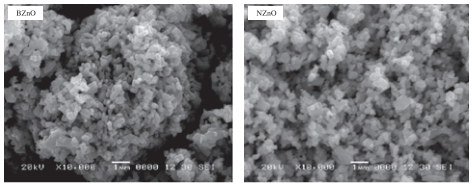

B-doped ZnO and N-doped ZnO synthesized by mechanochemical method were characterized by various techniques. Solar photocatalytic degradation of Bisphenol-A is in the order of B-ZnO > N-ZnO > ZnO.

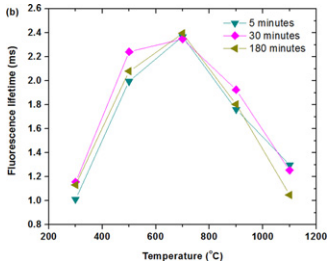

Fluorescence lifetimes of Eu-doped Y_2O_3 precursors heated for 5, 30, and 180 min to various temperatures.

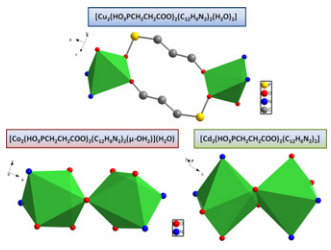

In same synthetic conditions, both the chemical and structural features of three transition metal(II) coordination polymers based on 2-carboxyethylphosphonate and 1-10′-phenanthroline are influenced by the metal cation characteristics, leading to non-homologous materials with different properties, which show the high chemical versatility of this interesting system.

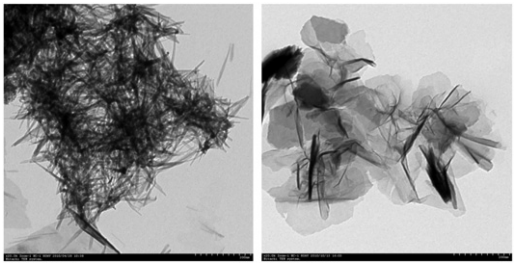

A facile solution-phase route has been developed to synthesize α-$Co(OH)_2$ nanorods and nanoplates. The possible growth mechanism of nanorods and nanoplates was proposed.

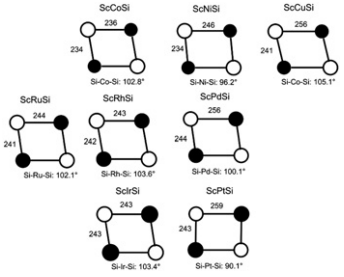

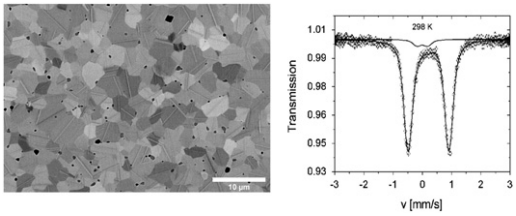

The vibrational polished $La_2Ni_{0.9}Fe_{0.1}O_{4+\delta}$ membrane revealed formation of secondary phases, which were confirmed by Mössbauer spectroscopy.

Continued

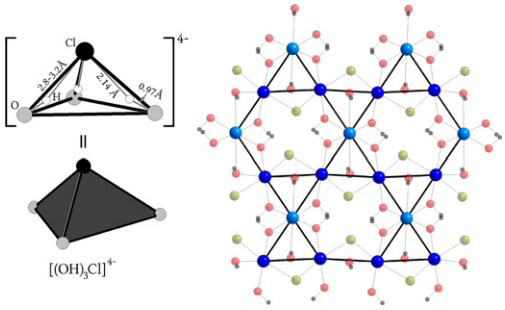

The $[(OH)_3Cl]^{4-}$ pseudopolyatomic anion and the kagomé lattice of $CdCu_3[(OH)_3Cl]_2$.

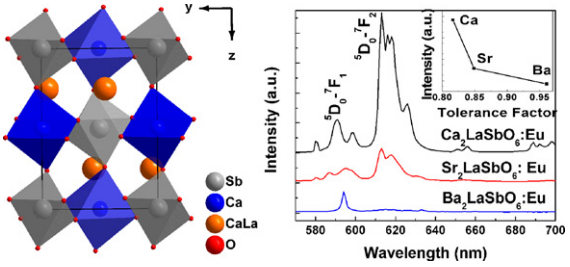

Eu^{3+} doped double-perovskite compounds A_2LnMO_6 (A = Ca, Sr, Ba; Ln = La, Gd, Y; M = Sb, Nb, Ta) show the dependence of luminescence intensity on the crystal structure.

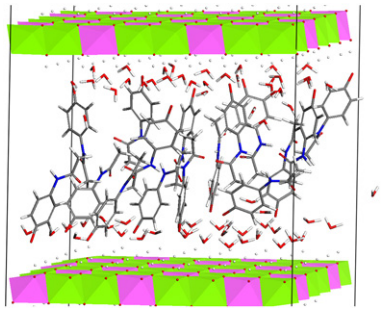

Molecular simulations showed disordered arrangement of paracetamol molecules in the interlayer; most of the interlayer water molecules are located near the hydroxide sheets.

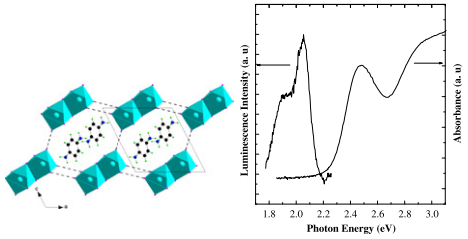

The structure of α-$[C_6H_4(NH_3)_2]_2Bi_2I_{10}$ consists of p-phenylenediammonium dications and dimeric decaiodobismuthate tetraanions stacked in a chessboard fashion. The optical properties were investigated by optical absorption and photoluminescence measurements.

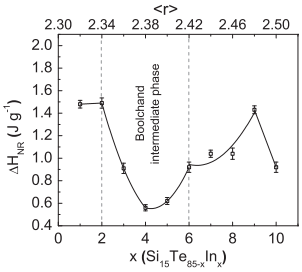

The variation of non-reversing heat flow (ΔHNR) of $Si_{15}Te_{85-x}In_x$ glasses with composition (x) and average coordination number ($\langle r \rangle$). The Boolchand intermediate phase can be seen in the composition range $2 \leq x \leq 6$.

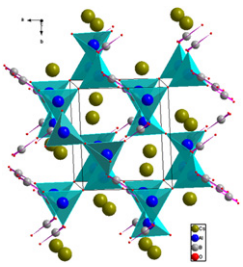

A new borate, $Cs_2Al_2B_2O_7$, was synthesized. In the structure, BO_3 triangles and AlO_4 tetrahedra are connected to form a three-dimensional framework with Cs^+ in the channels.

A practical grinding-assisted dry synthesis of nanocrystalline $NiMoO_4$ polymorphs for oxidative dehydrogenation of propane

Miao Chen, Jia-Ling Wu, Yong-Mei Liu, Yong Cao, Li Guo, He-Yong He and Kang-Nian Fan

page 3357

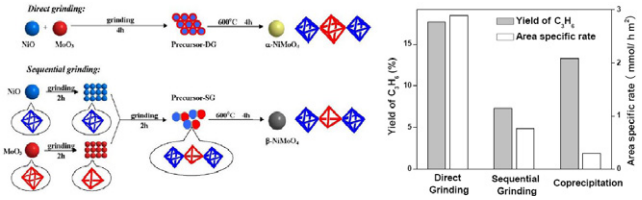

Grinding-assisted synthesis of $NiMoO_4$ offers higher and more reproducible activities in contrast to coprecipitation for oxidative dehydrogenation of propane, and both α- and β-$NiMoO_4$ can be synthesized.

Size effect of added LaB_6 particles on optical properties of LaB_6/Polymer composites

Yifei Yuan, Lin Zhang, Lijie Hu, Wei Wang and Guanghui Min

page 3364

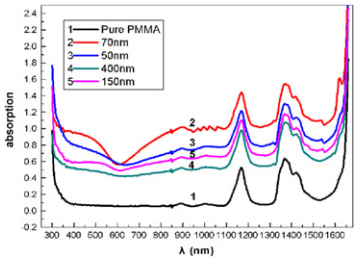

70 nm LaB_6 particles resulted in the best performance on absorption of VIS and NIR, which could not be apparently achieved by LaB_6 particles beyond nano-scale.

For a full and complete Guide for Authors, please go to: http://www.elsevier.com/locate/jssc

Journal of Solid State Chemistry has no page charges.

Continued